Received: 23 May 2024 | Accepted: 30 July 2024

DOI: 10.1002/pamm.202400137

RESEARCH ARTICLE

Topology optimization for precipitation hardening in ferroelectric material

Matthias Bohnen | **Ralf Müller**

Institute for Mechanics, Technical University of Darmstadt, Darmstadt, Germany

Correspondence
Matthias Bohnen, Institute for Mechanics, Technical University of Darmstadt, Darmstadt, Germany.
Email: matthias.bohnen@tu-darmstadt.de

Funding information
DFG, Grant/Award Number: 528293120

Abstract

Recent studies have shown that precipitation hardening effectively enhances the mechanical quality factor of ferroelectric material. In this work, Li-doped $NaNbO_3$, a material system with elliptical precipitates is investigated. We present a mechanical model to determine energetically stable precipitate shapes by minimizing the total energy, consisting of elastic and interface energy. Furthermore, we investigate the influence of external loads on the precipitate topology. Correct elastic constants as well as lattice misfits for the simulation are provided. The shapes determined from finite element simulations agree well with observed results.

1 | INTRODUCTION

Ferroelectric materials are of great importance for a variety of sensors and actuators, relating electrical, and mechanical fields in technical applications such as microelectronics, medical diagnostics or electronic devices in automobile industry [1]. Lead Zirconate Titanate (PZT) is a prominently used material because of its relatively large coupling coefficients and good performance at high temperatures. However, due to the well known toxicity of lead, the replacement of PZT is a topic of active research. Recent studies [2–4] investigate Li-doped $NaNbO_3$ as a lead-free alternative. Furthermore, these studies propose the technique of precipitation hardening, which is well known from metal processing. For application in ferroelectric material, supersaturated, orthorhombic $NaNbO_3$ is subjected to an aging process, which leads to the precipitation of hexagonal $LiNbO_3$ in the matrix. This effectively hinders domain wall motion due to pinning at the precipitates, leading to a reduced heat loss and thus higher mechanical quality factor of the new ferroelectric material. In ref. [4] the morphology and topology of the matrix-precipitate-system was investigated. However, determining the optimal shape and size of the precipitates remains an open question. This paper presents a mechanical model to determine energetically stable precipitates for the given material system. Furthermore we are interested in the influence of external mechanical load on the precipitate topology. The model is introduced in Section 2. To be self-consistent, we derive the elastic constants in Section 2.2 and quantify the lattice misfit of the crystalline phases in Section 2.3.

2 | GEOMETRY OPTIMIZATION

2.1 | Mechanical model

The schematic model for different two-dimensional matrix-precipitate systems is given in Figure 1. The grey lines indicate the pseudocubic axis system of the matrix material. The total energy consists of an elastic and an interface contribution, as

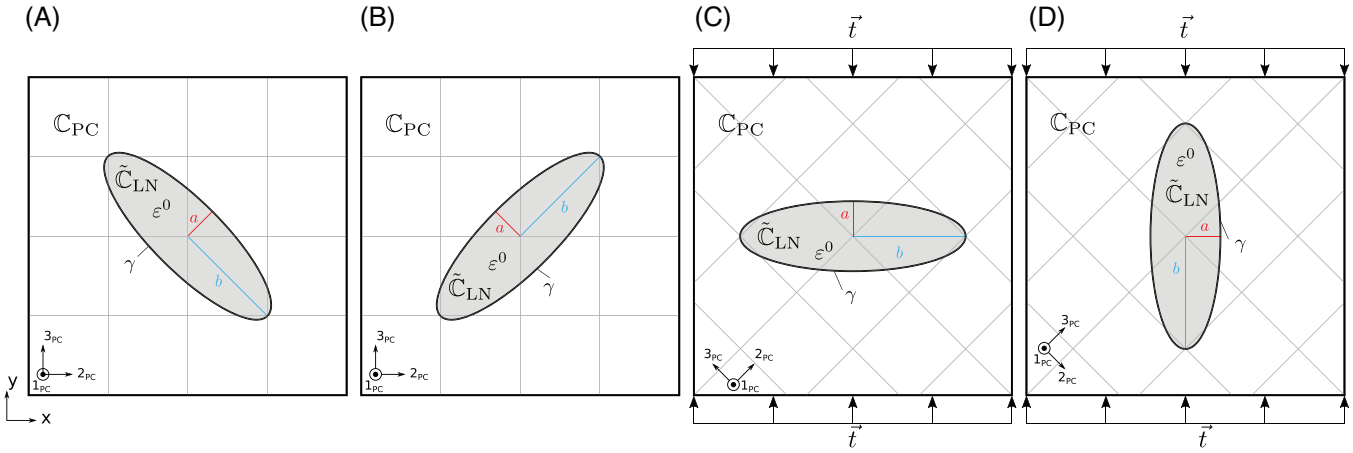

FIGURE 1 Matrix-precipitate-system for (A) variant I and (B) variant II as described in ref. [4]. (C, D) Models for systems under load with precipitate orientated parallel or perpendicular to load direction. Grey lines indicate the pseudocubic axis of the matrix material.

well as the potential of the external forces. We define a two-dimensional body that comprises of an infinite matrix domain M and a precipitate domain P, with interface Γ. We assume plane strain conditions. Due to the lattice misfit of the different crystal systems, an eigenstrain field $\boldsymbol{\varepsilon}_0$ is present in the precipitate domain, as derived in Section 2.3. Furthermore, to model the interatomic forces between the two materials at the interface, we define a surface energy density γ on Γ. The internal energy then reads

$$E_{\text{int}} = \int_{\text{P}\cup\text{M}} \frac{1}{2}(\boldsymbol{\varepsilon} - \boldsymbol{\varepsilon}_0) : \mathbb{C}(\boldsymbol{\varepsilon} - \boldsymbol{\varepsilon}_0)\, \mathrm{d}A + \int_{\Gamma} \gamma \mathrm{d}s, \tag{1}$$

with $\boldsymbol{\varepsilon}$ as the infinitesimal strain tensor, $\mathbb{C} = \mathbb{C}(\vec{x})$ the local fourth order stiffness tensor and $\mathrm{d}A$ and $\mathrm{d}s$ the infinitesimal surface and line element respectively. The stiffness tensor distinguishes between matrix and precipitate phase such as

$$\mathbb{C}(\vec{x}) = \begin{cases} \mathbb{C}_{\text{PC}} & \text{for } \vec{x} \in \text{M} \\ \tilde{\mathbb{C}}_{\text{LN}} & \text{for } \vec{x} \in \text{P} \end{cases}, \tag{2}$$

with the respective tensors derived in Section 2.2. The interface energy density is assumed to be isotropic and set to the constant value of

$$\gamma = 0.38 \frac{\text{J}}{\text{m}^2}. \tag{3}$$

If external loads are present on the boundary ∂M, they contribute to the total energy as

$$E_{\text{ext}} = -\int_{\partial\text{M}} \vec{t} \cdot \vec{u}\, \mathrm{d}s, \tag{4}$$

with the traction vector $\vec{t}$ and the displacement $\vec{u}$. Thus, the total energy of the system reads

$$E_{\text{tot}} = E_{\text{int}} + E_{\text{ext}}. \tag{5}$$

From ref. [4], the cross section of the precipitate is determined to $\tilde{A} = 8042\,\text{nm}^2$. By restricting the cross section A of the precipitate to a fixed value $A = \tilde{A}$, Equation (5) presents a minimization problem with the shape of the precipitate as degree of freedom. In this work, we restrict the precipitate to be purely elliptic and characterize it by its normalized aspect ratio

$$m = \frac{a - b}{a + b}, \tag{6}$$

where a and b denote the semi axis of the ellipsis. A finite element model is used to compute E_{tot} of Equation (5) for a given aspect ratio. The aspect ratio m is adjusted by an optimization routine to yield the optimal value m_{opt}. In particular, we make use of the finite element library from the FEniCS Project [5–14] as well as the optimization algorithm COBYLA provided by the SciPy library [15]. For mesh generation, we use the open source finite element mesh generator GMSH [16].

2.2 | Elastic constants

We are focusing on the material presented in ref. [4]. Here, hexagonal $LiNbO_3$ (LN) precipitates out of the orthorhombic $NaNbO_3$ matrix (NN). For convenience, NN is transformed to a pseudocubic crystal system (PC). The transformation (7) is formulated in Miller indices by denoting the parallelism of (hkl) crystal planes and $[hkl]$ directions with a "//"-symbol:

$$[100]_{\text{NN}} // [100]_{\text{PC}}, \tag{7a}$$

$$(002)_{\text{NN}} // (0\bar{1}1)_{\text{PC}}, \tag{7b}$$

$$(020)_{\text{NN}} // (011)_{\text{PC}}. \tag{7c}$$

Due to the different crystal systems and lattice parameters of PC and LN, the precipitation happens along lattice planes that yield the lowest lattice misfit at the interface. From a mechanical point of view, the lattice of LN is rotated in space to fit into the NN lattice. As the pseudocubic matrix offers three dimensional symmetry, multiple precipitation planes can be identified. Thus, in a two-dimensional view, four different variants of precipitates were observed in ref. [4]. In this work, we focus on the crystallographically equivalent variants I and II. Their orientation in space is given by relation (8).

$$[100]_{\text{PC}} // [241]_{\text{LN}}, \tag{8a}$$

$$(0\bar{1}1)_{\text{PC}} // (\bar{2}10)_{\text{LN}}, \tag{8b}$$

$$(011)_{\text{PC}} // (01\bar{4})_{\text{LN}}. \tag{8c}$$

Section 2.3 presents the calculation of the lattice misfit corresponding to relation (8). Due to the anisotropic misfit, the shape of the precipitate appears to be plate-like with an elliptic cross section projected along $[100]_{\text{PC}}$. In this plane, the two crystallographically equivalent precipitate variants are inclined by 45° and perpendicular to each other, as sketched in Figure 1A,B. For the computation of the mechanical energy introduced in Section 2, one must transform the elastic constants of LN to the PC system, whose basal vectors are parallel to the global coordinate system. In crystallography, the basal vectors of a unit cell are denoted by $\vec{a}$, $\vec{b}$, and $\vec{c}$. The stiffness for pure LN with respect to $\vec{a}_{\text{LN}}$, $\vec{b}^*_{\text{LN}}$, $\vec{c}_{\text{LN}}$, where $\vec{b}^*_{\text{LN}} = \vec{c}_{\text{LN}} \times \vec{a}_{\text{LN}}$, can be found in ref. [17] as

$$\underline{\mathbb{C}}_{\text{LN}} = \begin{pmatrix} C_{11} & C_{12} & C_{13} & C_{14} & 0 & 0 \\ & C_{11} & C_{13} & -C_{14} & 0 & 0 \\ & & C_{33} & 0 & 0 & 0 \\ & & & C_{44} & 0 & 0 \\ & \text{sym.} & & & C_{44} & C_{14} \\ & & & & & C_{66} \end{pmatrix}, \quad C_{66} = \frac{C_{11} - C_{12}}{2}. \tag{9}$$

Voigt notation is used denoted by an underbar. The plane relations (8) call for a change of basis for the stiffness tensor (9) to transform the elastic constants of LN to the PC system. Fundamental basics on tensor algebra can be found in ref. [18]. The relations (8) are casted into a system of equations such as

$$\underbrace{\begin{pmatrix} 1 & 0 & 0 \\ 0 & -1 & 1 \\ 0 & 1 & 1 \end{pmatrix}}_{\boldsymbol{N}} = \boldsymbol{A}^{-1} \underbrace{\begin{pmatrix} 2 & -2 & 0 \\ 4 & 1 & 1 \\ 1 & 0 & -4 \end{pmatrix}}_{\boldsymbol{L}}, \tag{10}$$

where $\boldsymbol{A} = \boldsymbol{LN}^{-1}$ presents the mapping of LN basal vectors to the PC system. As the transformation for the stiffness tensor requires an orthonormal basis we perform

$$\vec{a} = \boldsymbol{A} \cdot \begin{pmatrix} 1 \\ 0 \\ 0 \end{pmatrix} \rightarrow \tilde{\vec{a}} = \frac{1}{||\vec{a}||}\vec{a} \tag{11a}$$

$$\vec{c} = \boldsymbol{A} \cdot \begin{pmatrix} 0 \\ 0 \\ 1 \end{pmatrix} \rightarrow \tilde{\vec{c}} = \frac{1}{||\vec{c}||}\vec{c} \tag{11b}$$

$$\tilde{\vec{b}}^{*} = \tilde{\vec{c}} \times \tilde{\vec{a}}. \tag{11c}$$

and compose the transformation matrix as

$$\tilde{\mathbf{A}} = \begin{pmatrix} \tilde{\vec{a}} & \tilde{\vec{b}}^{*} & \tilde{\vec{c}} \end{pmatrix}. \tag{12}$$

The transformation of the fourth order stiffness tensor in index notation reads

$$\tilde{\mathbb{C}}_{ijkl} = \tilde{A}_{mi}\tilde{A}_{nj}\tilde{A}_{ok}\tilde{A}_{pl}\mathbb{C}_{mnop}, \tag{13}$$

which yields the final set of elastic constants for LN with

$$\underline{\tilde{\mathbb{C}}}_{\mathrm{LN}} = \begin{pmatrix} 197.15 & 54.32 & 73.26 & 3.8 & -0.15 & 6.28 \\ & 206.39 & 75.47 & -0.13 & -6.78 & 5.84 \\ & & 205.78 & 17.32 & -1.65 & -6.05 \\ & & & 68.47 & -3.13 & -2.32 \\ & \text{sym.} & & & 72.22 & -7.13 \\ & & & & & 62.82 \end{pmatrix} \text{GPa}. \tag{14}$$

As the pseudocubic matrix coincides with the global coordinate system, no transformation is required. We chose the values from [19] and assemble the stiffness tensor as

$$\underline{\mathbb{C}}_{\mathrm{PC}} = \begin{pmatrix} 235 & 110 & 110 & 0 & 0 & 0 \\ & 235 & 110 & 0 & 0 & 0 \\ & & 235 & 0 & 0 & 0 \\ & & & 77 & 0 & 0 \\ & \text{sym.} & & & 77 & 0 \\ & & & & & 77 \end{pmatrix} \text{GPa}. \tag{15}$$

For the investigation of the influence of external loads, the material system faces another in-plane rotation with

$$\boldsymbol{R} = \begin{pmatrix} \cos\varphi & -\sin\varphi & 0 \\ \sin\varphi & \cos\varphi & 0 \\ 0 & 0 & 1 \end{pmatrix}, \tag{16}$$

with $\varphi \pm 45^{\circ}$ as can be seen in Figure 1C,D. The following modeling is performed in two dimensions only and we select the 2-3-plane to model the mentioned precipitate variants I and II.

2.3 | Lattice misfit

To model the lattice misfit, we first compute the interplanar spacing of the crystal planes of the two phases meeting at the interface, widely denoted as the d-spacing. We use the formulas provided by ref. [20], which read for orthorhombic

TABLE 1 Interplanar spacing of matrix and precipitate phase.

	PC	LN	δ
a	3.8721 Å	5.1501 Å	
b	3.9046 Å	5.1501 Å	
c	3.9046 Å	13.8639 Å	
$d_{0\bar{1}1}$	2.7610 Å		
$d_{\bar{2}10}$		2.5750 Å	−0.0673
$d_{01\bar{4}}$		2.7368 Å	−0.0088

Abbreviation: PC, pseudocubic crystal system.

systems

$$\frac{1}{d^2} = \frac{h^2}{a^2} + \frac{k^2}{b^2} + \frac{l^2}{c^2} \tag{17}$$

and for the hexagonal systems

$$\frac{1}{d^2} = \frac{4}{3}\left(\frac{h^2 + hk + k^2}{a^2}\right) + \frac{l^2}{c^2}, \tag{18}$$

where a, b, c represent the lattice parameters of the respective unit cell and h, k, l the Miller indices of the plane under consideration. According to ref. [21], the lattice misfit δ is computed as the relative difference of the precipitate spacing with respect to the matrix spacing:

$$\delta = \frac{d_\mathrm{P} - d_\mathrm{M}}{d_\mathrm{M}}. \tag{19}$$

The lattice parameters of pseudocubic NN and hexagonal LN are given in ref. [4]. The interfacial misfits for the lattice planes given in the plane relations (8) are presented in Table 1. From the misfit values, the eigenstrain tensor with respect to the semi-major and semi-minor axes of the ellipsis is composed and assumed constant in the precipitate domain:

$$\boldsymbol{\varepsilon}_\mathrm{LN} = \begin{pmatrix} -0.0673 & 0 \\ 0 & -0.0088 \end{pmatrix}. \tag{20}$$

This tensor needs to be transformed to the global coordinate system with the transformation formula:

$$\varepsilon_{0_{ij}} = R_{ik} R_{jk} \varepsilon_{LN_{kl}}, \tag{21}$$

with R_{ij} from Equation (16). This yields the final eigenstrain tensor with respect to the PC system

$$\boldsymbol{\varepsilon}_0 = \begin{pmatrix} -0.03805 & 0.029 \\ 0.029 & -0.03805 \end{pmatrix}. \tag{22}$$

3 | SIMULATION RESULTS

3.1 | Energetically stable precipitate shapes

The model is verified by simulating a system with variant I like in Figure 1A. Starting from a circular inclusion, the dashed line in Figure 2 shows the evolution of the aspect ratio m versus the iteration steps. Larger negative values for m indicate an elongation of the ellipsis along its b-axis, with a final value $m_\mathrm{opt} = -0.870$, which is equivalent to $b/a = 14.38$. This agrees well with the measured value of 14 in ref. [4]. The solid lines show the evolution of the energy contributions versus the optimization steps. Due to the anisotropic eigenstrain, precipitates with large aspect ratios are energetically more favorable which can be seen from the plot of the total energy, which is closely related to the elastic energy reduction.

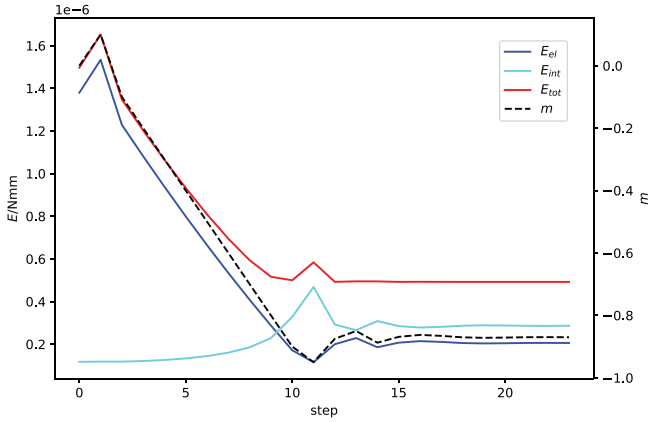

FIGURE 2 E_{el}: elastic energy, E_{int}: interface energy, E_{tot}: total energy, m: aspect ratio versus iteration step for precipitate variant I.

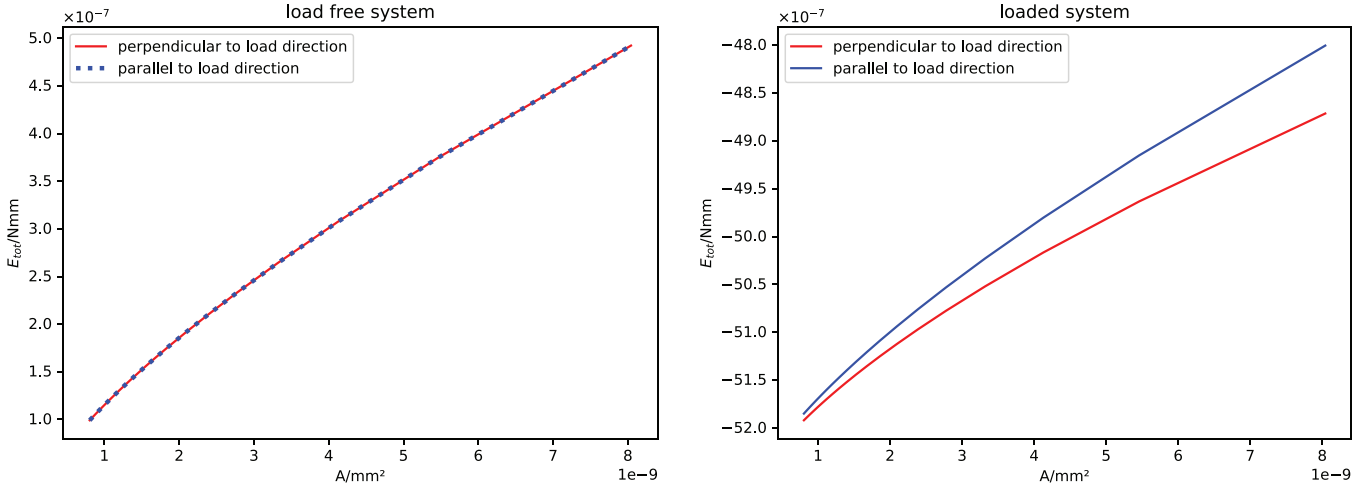

FIGURE 3 Total energy curves for matrix-precipitate-systems for (A) free boundaries, (B) loaded boundaries.

Increasing the aspect ratio goes along with an increase of interface energy. However, all curves are reaching stationary values towards the end of the optimization, indicating that an energetically stable precipitate shape was found.

3.2 | Influence of external loads

To investigate the influence of external loads on the precipitate geometry, we model two extreme cases in which the precipitate is oriented parallel or perpendicular to the load direction, as given in Figure 1C,D. For this purpose, the material properties are subjected to an in-plane rotation as described in Section 2.2. We repeat the simulations for different precipitate sizes and compare the total energy curves. Figure 3A yields that in the load-free case, the total energies of horizontal and vertical precipitate are equal. This agrees well with the observation of the crystallographically equivalent precipitate variants I and II in ref. [4]. However, if the system faces a vertical compression, the precipitate variant that is aligned perpendicular to the load direction appears to be energetically more favorable due to a lower total energy. Note that the sign of the energy changes due to the contribution of the work of the external forces. This holds for all precipitate sizes, as the energy difference becomes even larger with growing precipitate size. This can be attributed to a growing elastic energy contribution of the anisotropic eigenstrain field, which competes with the energy of the external forces. If the principle strain direction of the greatest principle strain is aligned parallel to the load direction, the configuration is more favorable.

4 | CONCLUSION

Motivated by the precipitation hardening technique for application on ferroelectric material, the present work proposes a model to compute energetically stable precipitate shapes by finding the minimal mechanical energy for a free aspect ratio. In particular, we investigate Li-doped $NaNbO_3$, for which elliptical precipitates were observed in previous studies. In principle, the approach presented in this work can be applied to other crystalline material as well. Based on a well defined morphology and crystal orientation for the exemplary material, this work includes an approach for a correct definition of elastic constants as well as lattice misfit. The anisotropic eigenstrain resulting from the lattice misfit is mostly responsible for the optimal aspect ratio of the precipitates and the determined shape agrees well with the observed results. Furthermore, if a load is applied to the system, the model yields that precipitates are energetically more favorable if the principle strain direction is aligned parallel to the load direction.

ACKNOWLEDGMENTS

Many thanks to Prof. Jürgen Rödel and his research group from the Department of Materials and Earth Sciences at TU Darmstadt for the helpful exchange as well as the Lichtenberg II Cluster in Darmstadt for supporting the computations. Financial support by the DFG for the project 528293120 is appreciated.

Open access funding enabled and organized by Projekt DEAL.

ORCID

Matthias Bohnen https://orcid.org/0009-0006-5166-1337

REFERENCES

1. Rödel, J., Webber, K. G., Dittmer, R., Jo, W., Kimura, M., & Damjanovic, D. (2015). Transferring lead-free piezoelectric ceramics into application. *Journal of the European Ceramic Society*, *35*(6), 1659–1681.
2. Zhao, C., Gao, S., Yang, T., Scherer, M., Schultheiß, J., Meier, D., Tan, X., Kleebe, H., Chen, L., Koruza, J., & Rödel, J. (2021). Precipitation hardening in ferroelectric ceramics. *Advanced Materials*, *33*(36), 2102421.
3. Zhao, C., Gao, S., Kleebe, H., Tan, X., Koruza, J., & Rödel, J. (2022). Coherent precipitates with strong domain wall pinning in alkaline niobate ferroelectrics. *Advanced Materials*, *34*(38), 2202379.
4. Gao, S., Zhao, C., Bohnen, M., Müller, R., Rödel, J., & Kleebe, H. J. (2023). Precipitate-domain wall topologies in hardened Li-doped NaNbO3. *Acta Materialia*, *254*, 118998.
5. Alnaes, M. S., Blechta, J., Hake, J., Johansson, A., Kehlet, B., Logg, A., Richardson, C., Ring, J., Rognes, M. E., & Wells, G. N. (2015). The FEniCS project version 1.5. *Archive of Numerical Software*, *3*. https://doi.org/10.11588/ans.2015.100.20553
6. Logg, A., Mardal, K., & Wells, G. N. (2012). *Automated solution of differential equations by the finite element method: The FEniCS book*. Springer.
7. Alnaes, M. S., Logg, A., Ølgaard, K. B., Rognes, M. E., & Wells, G. N. (2014). Unified form language: A domain-specific language for weak formulations of partial differential equations. *ACM Transactions on Mathematical Software*, *40*, 1–37.
8. Logg, A., & Wells, G. N. (2010). DOLFIN: automated finite element computing. *ACM Transactions on Mathematical Software*, *37*, 1–28.
9. Logg, A., Wells, G. N., & Hake, J. (2012). DOLFIN: a C++/Python finite element library. In A. Logg, K. Mardal, & G. N. Wells (Eds.),. *Automated solution of differential equations by the finite element method* (Vol. 84). Springer.
10. Kirby, R. C., & Logg, A. (2006). A compiler for variational forms. *ACM Transactions on Mathematical Software*, *32*, 417–444.
11. Logg, A., Ølgaard, K. B., Rognes, M. E., & Wells, G. N. (2012). FFC: the FEniCS form compiler. In A. Logg, K. Mardal, & G. N. Wells (Eds.). *Automated solution of differential equations by the finite mlement method* (Vol. 84). Springer.
12. Ølgaard, K. B., & Wells, G. N. (2010). Optimisations for quadrature representations of finite element tensors through automated code generation. *ACM Transactions on Mathematical Software*, *37*, 1–23.
13. Kirby, R. C. (2004). Algorithm 839: FIAT, a new paradigm for computing finite element basis functions. *ACM Transactions on Mathematical Software*, *30*, 502–516.
14. Kirby, R. C. (2012). FIAT: numerical construction of finite element basis functions. In A. Logg, K. Mardal, & G. N. Wells (Eds.), *Automated solution of differential equations by the finite element method* (Vol. 84). Springer.
15. Virtanen, P., Gommers, R., & Oliphant, T. E. (2020). SciPy 1.0: fundamental algorithms for scientific computing in Python. *Nature Methods*, *17*(3), 261–272.
16. Geuzaine, C., & Remacle, J. (2009). Gmsh: A 3-D finite element mesh generator with built-in pre- and post-processing facilities. *International Journal for Numerical Methods in Engineering*, *79*(11), 1309–1331.
17. Ogi, H., Kawasaki, Y., Hirao, M., & Ledbetter, H. (2002). Acoustic spectroscopy of lithium niobate: Elastic and piezoelectric coefficients. *Journal of Applied Physics*, *92*(5), 2451–2456.
18. Tadmor, E. B., Miller, R. E., & Elliott, R. S. (2011). *Continuum mechanics and thermodynamics: From fundamental concepts to governing equations* (1st ed.). Cambridge University Press.

19. Tomeno, I., Tsunoda, Y., Oka, K., Matsuura, M., & Nishi, M. (2009). Lattice dynamics of cubic NaNbO 3: An inelastic neutron scattering study. *Physical Review B*, *80*(10), 104101.
20. Wadhwa, A. S., & Dhaliwal, H. S. (2008). *A textbook of engineering material and metallurgy*. University Science Press.
21. Jain, S. C., Harker, A. H., & Cowley, R. A. (1997). Misfit strain and misfit dislocations in lattice mismatched epitaxial layers and other systems. *Philosophical Magazine A*, *75*(6), 1461–1515.

How to cite this article: Bohnen, M., & Müller, R. (2024). Topology optimization for precipitation hardening in ferroelectric material. *Proceedings in Applied Mathematics and Mechanics*, *24*, e202400137. https://doi.org/10.1002/pamm.202400137